

Microstructural evolution of mechanically deformed polycrystalline silicon for kerfless photovoltaics

M. Wu¹, J.D. Murphy^{2,1*}, J. Jiang^{3,1}, P.R. Wilshaw¹, A.J. Wilkinson¹

¹ Department of Materials, University of Oxford, Parks Road, Oxford, OX1 3PH, UK

² School of Engineering, University of Warwick, Coventry, CV4 7AL, UK

³ Department of Mechanical Engineering, Imperial College London, London SW7 2AZ, UK

* Corresponding author: john.d.murphy@warwick.ac.uk

Keywords: silicon; photovoltaics; dislocations; electron backscatter diffraction, deformation

Abstract

Silicon wafers for photovoltaics could be produced without kerf loss by rolling, provided sufficient control of defects such as dislocations can be achieved. Here we report a study using mainly high resolution electron backscatter diffraction (HR-EBSD) of the microstructural evolution of Siemens polycrystalline silicon feedstock during a series of processes designed to mimic high temperature rolling. The starting material is heavily textured and annealing at 1400 °C results in 90% recrystallization and a reduction in average geometrically necessary dislocation (GND) density from $>10^{14} \text{ m}^{-2}$ to 10^{13} m^{-2} . Subsequent compression at 1150 °C – analogous to rolling – produces sub-grain boundaries seen as continuous curved high GND content linear features spanning grain interiors. Post-deformation annealing at 1400 °C facilitates a secondary recrystallization process, resulting in large grains typically of 100 μm diameter. HR-EBSD gives the final average GND density in as $3.2 \times 10^{12} \text{ m}^{-2}$. This value is considerably higher than the dislocation density of $5 \times 10^{10} \text{ m}^{-2}$ from etch pit counting, so the discrepancy was investigated by direct comparison of GND maps and etch pit patterns. The GND map from HR-EBSD gives erroneously high values at the method's noise floor ($\sim 10^{12} \text{ m}^{-2}$) in regions with low dislocation densities.

1. Introduction

Currently about 90% of photovoltaic (PV) solar cells are based on crystalline silicon technologies. Cells are mainly produced from wafers sawn from ingots produced by the Czochralski process or directional solidification. A substantial proportion (up to 50%^[1]) of the silicon material is lost during the wafering process. Although some efforts have been made to recover lost material,^[2] the fact remains that energy and feedstock are wasted on producing high quality material which never ends up in a solar cell.

Various groups have studied the production of so-called *kerfless* silicon, which does not require the cutting of wafers and hence could result in more efficient material usage.^[3] Approaches investigated include epitaxial foils,^[4-6] ribbon growth,^[7, 8] and sintering.^[9] An alternative method for rapid and cost-effective silicon sheet fabrication is via hot mechanical rolling. Hot deformation of silicon was attempted in the late 1970s and early 1980s, and was found to be promising from a mechanical perspective.^[10-12] Polycrystalline silicon can be uniaxially compressed by as much as 50% at 1380 °C at a strain rate of 7 s⁻¹ without cracking.^[11] However, the work was discontinued due to the extremely poor minority carrier lifetime in the material produced.^[13] We are re-visiting the potential of mechanically deformed silicon for PV. Initially, as constructing a clean high temperature rolling rig is a major challenge, we are using uniaxial compression to mimic the effect of rolling and to generate similar crystal defects. Our compression set-up operate under clean conditions. As earlier deformation studies were carried out in metallurgical conditions^[10-13] with no apparent attempt to prevent contamination, we hope that our approach when combined with modern gettering and passivation processes will eventually result in wafers with adequate electronic properties.

This paper presents an initial study into the microstructural changes which occur during high temperature processing, including deformation, of silicon. We start with polycrystalline silicon produced by chemical vapour deposition (CVD) using the Siemens process,^[14] whose microstructural properties have been investigated only rarely (*e.g.* Ref. ^[15]) as the feedstock is usually first melted. The key structural defects to monitor are dislocations, as these correlate with a reduction in the silicon's minority carrier lifetime.^[16] Groups of dislocations in crystals can be classified into two different categories, namely, the statistically stored dislocations (SSDs) with net Burgers vector of zero over some Burgers circuit and geometrically necessary dislocations (GNDs) with non-zero net Burgers vector.^[17, 18] The distinction can only be made in terms of fractions of the total density of dislocations threading the Burgers circuit used for assessment rather than individual defects and is also inherently tied to the size of the Burgers circuit. GNDs are generated as excess dislocations accumulate to satisfy the geometrical compatibility during plastic deformation, and hence are

exclusively related to crystal lattice curvature.^[19] A high resolution electron backscatter diffraction (HR-EBSD) cross-correlation method has been developed which can measure GNDs in crystalline materials.^[20, 21] The HR-EBSD measurement relies on determining the deviation from positions in a reference pattern of a number of regions of interests (ROIs) in an electron backscatter diffraction pattern acquired from an array of points on the sample. Most of the work to-date has focussed on plastically-deformed metals (*e.g.* Refs ^[22, 23]), although polysilicon thin films for PV applications have also been studied,^[24] and conventional EBSD has recently been applied in an extensive microstructural study of cast multicrystalline Si.^[25] As well as HR-EBSD we also used other characterization methods, including preferential etching and secondary electron imaging using a focussed ion beam (FIB) for revealing overall surface microstructure, conventional electron backscatter diffraction (EBSD) to obtain crystallographic information, and transmission electron microscopy (TEM) to configure bulk defect morphology. This study represents an important first step in quantifying the microstructural changes which occur during hot rolling of silicon.

2. Materials, processing and characterisation methods

2.1 Materials

The starting material was polycrystalline silicon produced by the Siemens process in which grains grow radially outwards from a central single crystalline silicon rod in a CVD reactor chamber. The rod of silicon grows in size from about 0.5 cm in diameter to about 10 cm to 15 cm. The length of the rod was in the range of 1 m to 1.5 m. A sample with dimensions of 15 mm × 15 mm × 10 mm was cut from the material using a saw with a diamond wafering blade. The orientation relative to the polycrystalline silicon rod is shown in **Figure 1**. The 10 mm side coincides with the grain growth axis, *i.e.* the radial direction from the centre of the rod. A planar etch (comprising 8% HF (40%), 75% HNO₃ (69%) and 17% CH₃COOH) was applied at room temperature to remove residual saw damage with ~50 µm being removed from all surfaces.

2.2 Deformation and annealing

The sample was cleaned using a standard RCA process and then sealed in an RCA-cleaned high purity quartz ampule with a pure argon ambient. The sample-containing ampule was then annealed at 1400 °C for 30 min in a chamber furnace and slowly cooled down to room temperature in the furnace. The cooling profile is approximately 4 to 5 °C/ minute between 1400 °C and 200 °C, followed by 1 to 2 °C/ minute between 200 °C and room temperature. The function of this anneal is to reduce recrystallize the starting material and to reduce the dislocation content. The annealing time

was guided by a preliminary time-dependent study which found no appreciable difference in microstructure for peak temperature annealing times between 30 min to 120 min.^[26] The pre-annealed polycrystalline sample was then subjected to uniaxial compression by 10% at 1150 °C in a flowing argon ambient using pre-cleaned deformation components. The maximum stress applied was 100 MPa and the average strain rate was approximately $7 \times 10^{-6} \text{ s}^{-1}$. The loading direction was along the 10 mm side, which is parallel to the original grain growth axis (Figure 1). After deformation, the polycrystalline sample was mechanically sawn into 1 mm thick slices for microstructural investigation. Saw damage was removed from the surfaces using the planar etching process. These thin specimens were then cleaned and sealed in clean quartz ampules before being subjected to subsequent thermal treatments at 1400 °C for different times (15 min to 120 min). Results presented in this paper are from specimens whose surface normal is along the compression axis, apart from Figure 2 (a) whose surface normal is perpendicular to the compression axis.

2.3 Sample surface preparation and EBSD

The 1 mm specimens underwent three surface preparation steps for microstructural examination. First, a flat surface was obtained by grinding with silicon carbide paper. Second, the samples were polished progressively using 6 μm and 1 μm diamond pastes followed by a 50 nm colloidal silica slurry. Third, plasma cleaning using ionized nitrogen atoms was used to produce an ultra-clean surface for EBSD samples. EBSD patterns were acquired with TSL-EDAX orientation imaging microscopy (OIM) DC v5.3 software using a JEOL-6500F field emission scanning electron microscope operated at a beam energy of 20 keV, a probe current of up to ~16 nA and a sample tilt of 70°. A typical area of $100 \times 100 \mu\text{m}^2$ was scanned with a typical step size of 0.5 μm . EBSD patterns were recorded at the full $\sim 1 \times 1 \text{ pixel} \times 12 \text{ bit}$ deep resolution (no binning) of the Peltier-cooled CCD camera and saved for batch off-line analysis using code described previously.^[20, 27]

The analysis uses a cross-correlation based image processing method,^[20, 21] which provides ~100 times higher angular resolution improvement on the measurement of pattern shifts in acquired EBSD patterns comparing to conventional Hough-based EBSD method. The increased angular sensitivity enables the measurement of elastic distortions and sufficient sensitivity to determine GND content in the crystal. By comparing shifts relative to positions in a pattern from a selected reference point for all the test points within each grain, the deformation gradient matrix can be determined and this can be decomposed into the elastic strain and rotation using a standard continuum mechanics approach. A lower-bound estimate of the GND density based on Nye's theory^[17] can then be made by

determining the lattice rotation gradient (curvature). The details of this method have been published previously.^[20, 21, 28]

2.4 Etching and other microscopic characterisation

To reveal dislocations and grain boundaries some samples were subjected to a defect revealing etch after the colloidal silica polishing stage. Samples were placed in a Sirtl etch solution (0.3M CrO₃ and 40% HF in the ratio 5:4) for 30 s at room temperature. Etched samples were characterised using secondary electron imaging in an FEI FIB200 focussed ion beam (FIB) microscope with a gallium ion beam. Thin foils of silicon were extracted from the bulk for subsequent examination using TEM with a lift-out technique. Four major steps are involved in the lift-out process, namely platinum deposition (a 1 µm thick protective layer of platinum is deposited on the specific surface where the TEM specimen was chosen from), preliminary milling, delicate polishing and final lift-out. TEM thin foil specimens measuring 15 µm × 10 µm × 100 nm were fabricated using this technique. TEM examination was performed using a JEOL 2000FX operating at 200 kV.

3. Results

3.1 Microstructure of as-received Siemens polycrystalline silicon

Figure 2 shows FIB secondary electron images of the microstructure from etched surfaces (a) parallel and (b) perpendicular to the grain growth axis in the as-received Siemens polycrystalline material. An appreciable tree-stem-like structure elongated in the grain growth direction was observed (Figure 2 (a)). A few large primary tree-stem grains of up to 40 µm in diameter were revealed (Figure 2 (b)). The etch pit density in these grains was relatively low (of order 10¹¹ m⁻²).

Figure 3 shows EBSD maps acquired on samples cut perpendicular to the grain growth axis. Figure 3 (a) shows image quality (IQ) which gives an indication of the quality of specimen surface preparation as well as on grain boundary positions. Figure 3 (b) shows an inverse pole figure (IPF) map with Σ3 and Σ9 grain boundaries highlighted, indicating a high frequency of these two twin-related boundaries. The as-received microstructure comprises circular twinned grain clusters nucleated at discrete sites which grow radially outward from the central rod (see Figure 1). Within a circular cluster there are typically twinned grains separated by Σ3 and Σ9 boundaries. The cluster diameters generally range from 5 µm to 30 µm. The remaining matrix comprises small grains with more random orientations, with an average grain size of 1 µm or smaller.

3.2 Evolution of texture and GND density

Figure 4 shows IPF maps, IPFs, and corresponding GND density distribution maps determined by HR-EBSD cross-correlation analysis for samples at different stages of thermomechanical processing. Data are shown for three different polycrystalline silicon samples: (a) in the as-received state; (b) following a pre-deformation anneal for 30 min at 1400 °C; and (c) following deformation at 1150 °C by 10% plastic strain after the pre-deformation anneal for 30 min at 1400 °C.

The IPF maps show the crystallography along the macroscopic axis along the radial growth direction of the original CVD material which is also parallel with the compression axis. The as-grown material has preferential alignment of $\langle 110 \rangle$ axes along the growth direction with a peak intensity 3.0 times that for a random orientation distribution. Several of the multiply twinned regions share a common $\langle 110 \rangle$ axis that is along the radial direction and so appear green within the IPF map (Figure 4 (a)). The pre-deformation annealing significantly weakens the texture, with the preferred axis becoming $\langle 112 \rangle$ and the intensity dropping to a maximum value of 1.6 times random. This alignment strengthens to ~ 2.6 times random as a result of the compression.

Figure 4 (a) shows the GND density in the as-received state is very high. Visual assessment of the GND density map for the as-received silicon shows a large number of red GND density ‘hot spots’ with a local GND density in excess of 10^{14} m^{-2} and a lower number of ‘cold spots’, representing low GND content areas ($< 10^{14} \text{ m}^{-2}$), which appear to mostly correspond to the interiors of large twinned circular grains. The lower plot in Figure 4 (a) shows the statistical correlation between GND density and position in the sample relative to the nearest grain boundary. Points nearer to the map edge than a grain boundary segment captured in the map were rejected from the analysis. There is a tendency for the larger GND densities to be found closer to the grain boundaries, and the median GND density is higher close to the grain boundaries.

Figure 4 (b) shows that the 30 min anneal at 1400 °C before deformation has a dramatic effect on the material’s microstructure. Approximately 90 % of the polycrystalline material recrystallizes as a result of the process, estimated by visual assessment. The annealing process not only remarkably alters the general grain structure but also significantly reduces the GND content. The average GND density after pre-deformation annealing is $6.2 \times 10^{12} \text{ m}^{-2}$. Again visual assessment of the GND density map suggests that high GND density features tend to coincide with high angle grain boundaries (misorientation between adjacent grains $> 10^\circ$) with the exception of a few extremely high GND density clusters, presumably surviving from the as-received state. This trend is borne out by the statistical analysis showing a more marked decrease in median GND density with distance away

from the nearest grain boundary. The reduction in GND density and increase in grain size is also apparent in the correlation plot.

Figure 4 (c) shows maps from a sample subjected to the 1400 °C 30 min pre-anneal followed by the deformation process described above with the load applied perpendicular to the mapped surface. Direct visual qualitative inspection of the IPF maps shows no significant grain structure alteration after plastic deformation. However, the corresponding GND density distribution map reveals that a distinctive heterogeneous deformation microstructure has been formed during the process. A large number of continuous curved high GND density content linear structures were found, forming an extensive GND network. These linear structures are low angle subgrain boundaries, with misorientations just below the threshold 10° (0.17 rad) used to segment grains using the EBSD orientation data. The GND density stored in the dislocation features is generally of order 10^{14} m^{-2} , whereas between these features the GND density is approximately $5.0 \times 10^{13} \text{ m}^{-2}$. The trend of higher GND densities closer to grain boundaries is seen once more but deformation at the elevated temperature appear to have weakened the correlation compared to the annealed state.

The overall evolution of the GND distributions without considering the location where dislocations are stored can be observed in the histograms presented in **Figure 5**, in which the GND density frequency is plotted as a function of $\log_{10}(\rho_{\text{GND}})$, where ρ_{GND} is the area density of GNDs. The GND density of the as-received state (Figure 5 (a)) appears to be a log-normal type distribution, as per the inset. The inset plot is reasonably linear though a deviation to lower than expected probabilities is seen at the low density edge of the distribution. The reason for this is not currently clear. Upon pre-deformation annealing at 1400 °C for 30 min, the mean GND value was found to shift significantly towards the lower density side (Figure 5 (b)). However, two major peaks were observed in the GND density distribution, corresponding to the recrystallized regions and un-recrystallized debris. It is of interest to note that the lower GND density peak seems to fit well with the expectation of the noise floor ^[29]. After plastic deformation the GND density distribution appears approximately log-normal again and the effect of the lower GND density has diminished substantially (Figure 5 (c)).

The relationship between grain size and GND density is reported in **Figure 6**. To give a simple metric for grain size the equivalent circle diameter (D) was used, as calculated from the grain area (A) measured by EBSD using $D = 2 \times \sqrt{A/\pi}$. For each map, the dataset with range of 0 to 14 μm was grouped into 5 to 10 bins and data in each bin were sorted in descending order. The points at 50 % of

all points in each bin are plotted as red dot centile lines in Figure 6. These median lines are only marked when a minimum 20 grains were found within a bin.

The grain size in as-received samples is small and there is relatively little variation in GND density with grain size (Figure 6 (a)). 30 min annealing at 1400 °C creates a relatively strong inverse correlation between the grain average GND density and grain diameter, with higher GND densities tending to be present in smaller grains (Figure 6 (b)). The microstructure after plastic deformation at 1150 °C by 10% maintains this inverse non-linear correlation (Figure 6 (c)).

3.3 Microstructural evolution with post-deformation annealing

High temperature annealing was performed after deformation to reduce the defect content in the microstructure of the deformed sample. Unlike the pre-annealed case, the microstructure varied substantially in different regions of the sample. In some regions a secondary recrystallization had occurred but in others it has not. **Figure 7** shows IPF and GND density maps from different regions of a deformed sample annealed after deformation for 15 min at 1400 °C. In Figure 7 (a) no substantial secondary recrystallization had occurred; in (b) partial secondary recrystallization had occurred; and in (c) almost full secondary recrystallization had occurred. However, even within the area where secondary recrystallization did not occur (Figure 7 (a)), it is clear that the GND density generally decrease considerably from the as-deformed state to typical values of order 10^{13} m^{-2} . The high GND densities previously found in the grain interiors (Figure 4 (c)) have mostly been removed, even though the grain structure has not altered significantly from the as-deformed state.

Figure 7 (b) shows that in some partially recrystallized regions individual anomalously large recrystallized grains have been observed to be surrounded by small high GND content grains. These large recrystallized grains have been observed to have diameters up to $\sim 40 \text{ }\mu\text{m}$ and measured GND density of order 10^{12} m^{-2} . In contrast, the surrounding high GND content grains are typically approximately 5 to 10 μm across and contain extremely high GND densities ($> 10^{14} \text{ m}^{-2}$). In regions where the secondary recrystallization is more complete, such as in Figure 7 (c), the general grain morphology is altered significantly. Some very large ($> 70 \text{ }\mu\text{m}$ diameter) grains have been observed with low GND content. The GND density is noticeably more homogeneous across these recrystallized grains with an average value of $3.2 \times 10^{12} \text{ m}^{-2}$.

3.4 Comparison of HR-EBSD GND densities with preferential etching

GND density measurements from the cross-correlation HR-EBSD technique were compared with dislocation density measurements made by counting etch pits revealed by chemical etching

techniques. A partially-recrystallized region from a sample annealed at 1400 °C for 15 min after mechanical deformation was selected for a comparative study. The region selected for study had both high GND density and low GND density regions. **Figure 8** shows an EBSD image quality map, a GND density distribution map and an SEM micrograph after the defect-revealing etch for the same region. The EBSD image quality map with grain boundary type highlighted (Figure 8 (a)) reveals that the large central recrystallized grain is separated from the surrounding grains by high angle grain boundaries (marked as blue lines). However, the non-recrystallized surrounding regions contain a large number of low angle grain boundaries (marked by red lines). The high GND density features recovered by the cross-correlation method are in good agreement with low angle grain boundaries revealed by image quality map, as marked by black circles in Figure 8 (a) and 8 (b).

A more detailed comparison was conducted on two selected regions (red squares in Figure 8 (c)) using higher magnification. The corresponding micrographs of the preferentially-etched surface microstructure and associated GND distribution maps are shown in **Figure 9**. In high GND density regions (black rectangles), linear features with very high GND densities (up to 10^{15} m^{-2}) correspond to continuous sub-grain boundaries revealed by preferential etching. Red rectangles highlight the medium GND density area where the cross-correlation method reveals an approximate GND density of $3.2 \times 10^{13} \text{ m}^{-2}$ and etch pit counting gives a dislocation density with the same order of magnitude. Examination of the low GND content area reveals an average GND density of $3.2 \times 10^{12} \text{ m}^{-2}$, however, the number found by counting of etch pits is considerably lower than this value at less than 10^{11} m^{-2} .

In order to understand better the genuine dislocation density of the low GND content area, a thin foil TEM specimen was fabricated using a FIB lift-out technique from the centre of a large recrystallized grain. **Figure 10** (a) shows the location and side view of the TEM sample prior to lift-out. The top bright strip is a platinum layer deposited to protect the film from gallium ion beam damage in the FIB. Figure 10 (b) is a bright field TEM image taken with the foil tilted near the [111] zone axis. Twin grains were observed in the specimen and the average dislocation density estimated by TEM is of the order of 10^{11} m^{-2} . This value is consistent with the value obtained by etch pit counting of the same region, but again considerably lower than the GND density value of $3.2 \times 10^{12} \text{ m}^{-2}$ obtained by HR-EBSD. It is noted that TEM has limitations when quantifying the density of structural defects because of the relatively small volumes probed and also in this case the TEM foil is taken perpendicular to the surface studied by HR-EBSD. Differences in dislocation density measurements from the different techniques are discussed further in Section 4.3.

4. Discussion

4.1 Microstructure of Siemens polycrystalline silicon

The as-received Siemens polysilicon material has a very high concentration of in-grown defects. With conventional techniques it is difficult to extract statistically meaningful information on dislocation densities as etch pits overlap and the dislocation morphologies make TEM challenging. Cross-correlation analysis of the EBSD patterns has therefore proven effective in not only numerically quantifying GND content (Figure 4 (a)) but also providing important information on the relation between grain structure and spatial GND distribution (Figure 5 (a) and Figure 6 (a)).

A distinct inhomogeneous stem-tree-like microstructure was found in the as-received Siemens polycrystalline silicon (Figure 2 and Figure 3). Small grains appear to nucleate discretely at various locations and form large twin grains which are generally elongated in the grain growth direction (radially outward from the centre silicon rod). These small grains are formed due to the fast chemical vapour deposition process at a relatively low temperature. Our characterisation results for as-received polycrystalline silicon are broadly consistent with those from other studies.^[12, 30, 31] In previous reports, the $\langle 110 \rangle$ preferred growth orientation was not only observed in bulk CVD polycrystalline silicon,^[30] but also in polysilicon films produced by CVD method on different silicon substrates.^[32] It was suggested that the high surface energy of the (110) planes causes the crystallites to grow in the $\langle 110 \rangle$ direction, *i.e.* nucleation of $\{110\}$ islands is kinetically favoured.^[32] However, the surface microstructure of polycrystalline silicon in previous studies^[12, 30-32] was only examined qualitatively by optical metallography and the existence of growth twins was only inferred from the appearance of striated needle clusters. Our study provides a more direct characterisation of the defect morphology and crystallography. Using HR-EBSD (combined with chemical etching) we have also been able to quantify the GND density.

4.2 Evolution of microstructure with processing

The recrystallization behaviour of as-received polysilicon is consistent with previous studies but with a significantly shorter period of time.^[12, 30, 33] Schins *et al.* found that fine grained (0.1 μm to 10 μm) high purity bulk polycrystalline silicon grown by CVD can be recrystallized to larger oblong grains (20 μm to 2 mm in length and 20 μm to 100 μm in diameter) by 3 hours thermal treatment at elevated temperatures between 1350 °C and 1400 °C.^[30] Their starting material and annealing conditions are relatively similar to ours, but we find a much shorter time for nearly complete

recrystallization and more homogeneous microstructure with equiaxed grains in smaller average size (approximately 30 μm in diameter). In addition, in previous studies the primary $\langle 110 \rangle$ fibre texture of the as-grown materials was converted into a strong $\langle 111 \rangle$ texture with free rotation around this axis after recrystallization.^[30, 33] In comparison, despite the existence of some abnormal elongated grains in length of approximately 30 μm coinciding with the original grain growth direction in the recrystallization microstructure in the present study, we found no preferred $\langle 111 \rangle$ texture in the matrix by EBSD analysis. This can be possibly attributed to different grain growth profiles of the starting materials, leading to different numbers of grown-in crystalline defects which provide different levels of driving force upon high temperature annealing. A more similar thermal treatment of bulk polycrystalline silicon to the current study was conducted by Lall *et al.*^[12] In their investigation, as-grown CVD polysilicon was annealed at 1380 °C for 24 hours, resulting in a uniform microstructure with the removal of small grains which appears similar to our recrystallised microstructure (Figure 7).

The deformation and subsequent annealing of bulk polysilicon were studied by previous researchers under different conditions.^[10-12, 33] Recrystallization in both cast and CVD grown polycrystalline silicon after high temperature plastic deformation and subsequent annealing has been widely observed, and this is analogous to the behavior of metals. Kinoshina and Champier^[34, 35] conducted tensile tests on cast ‘Silso’ polycrystalline silicon^[36] between 800 °C and 1050 °C followed by heat treatments at around 1400 °C. It was found that 13% external tensile strain at 950 °C followed by subsequent annealing at 1395 °C for 4.5 hours led to approximately 50% of the material recrystallized, whereas 10% tensile strain at 1050 °C and subsequent annealing at 1396 °C for 10 days yielded a complete recrystallization of the deformed polysilicon. It was noted qualitatively that the recrystallization fraction is proportional to the initial strain, and temperature and time of subsequent annealing, irrespective of the strain rates. The resultant recrystallized grains range from 80 μm to 1.8 mm with dislocation densities in large recrystallized grains determined by etching to be between 10^7 m^{-2} and 10^8 m^{-2} , compared to the as-cast polysilicon which had a grain size ranging from 150 μm to 750 μm and a dislocation density between 10^{10} m^{-2} and 10^{12} m^{-2} .^[34] Whilst dislocation densities reported by Kinoshina and Champier in recrystallised material are significantly lower than ours, it is noted that their values are from within certain grains and their TEM results shows the dislocation densities to be much higher in many other regions. For comparison, our work on CVD-grown polysilicon compressed at 1150 °C by 10% achieved almost complete recrystallization upon annealing for just 2 hours at 1400 °C. The difference in behaviour is attributed to differences in growth methods of the feedstock materials. In as-cast polysilicon, the internal strain

is insufficient to promote initial recrystallization from the as-grown state, therefore an additional applied strain is required for recrystallization.

The study of Schins and Radelaar^[33] was performed on similar starting material to our current work. Their material was first subjected to 3 hours pre-annealing at 1350 °C to achieve an initial recrystallization followed by uniaxial tension at 1140 °C by 5%. A subsequent thermal treatment at 1390 °C induced secondary recrystallization which yielded large grains with size in order of 1 mm. The deformation and annealing temperatures are approximately equivalent to those we used. However, the time required for them to achieve a complete secondary recrystallization was between 20 and 34 hours. The difference in total induced strain by plastic deformation possibly accounts for the remarkably longer annealing time for their complete secondary recrystallization. TEM examination conducted in their work revealed a dislocation density of $2.0 \times 10^{13} \text{ m}^{-2}$ inside sub-grains in a sample compressed by 30% at 1270 °C. This value, however, is still approximately an order of magnitude lower than the one obtained in this work with only 10% strain. Another difference lies in the texture change throughout processing. In their work, the initial $\langle 110 \rangle$ fibre texture changed into a $\langle 111 \rangle$ fibre texture after the primary pre-annealing recrystallization. After compression along the original $\langle 110 \rangle$ orientation at 1120 °C and 1280 °C up to 30% the $\langle 111 \rangle$ fibre texture was changed into a deformation texture with a $\langle 110 \rangle$ axis parallel to the compression axis. This sort of texture change was not observed in our work.

Kulkarni and Graham *et al.* carried out plastic compression on CVD polysilicon at 1380 °C with various strain rates both along and normal to the original $\langle 110 \rangle$ fibre orientation.^[10, 11, 31] Their deformed polysilicon completed the recrystallization process after annealing at 1380 °C for 10 min when the sample was compressed perpendicular to the original $\langle 110 \rangle$ direction by 30% at 1380 °C. This finding is, to a certain extent, of equivalent timescale to the secondary recrystallization behaviour observed by us. They claimed their recrystallized material is textured with a $\langle 110 \rangle$ axis parallel to the compression axis and a $\langle 111 \rangle$ axis along the original $\langle 110 \rangle$ axis. However, it is worth noting that their starting polysilicon was subjected to a pre-annealing at 1380 °C for 20 min before plastic compression. The microstructure after pre-annealing was never examined and the possibility of a preliminary recrystallization introduced by this annealing treatment was never taken into account. It was speculated in their study that grain growth occurred without texture change during the pre-annealing. Since it is already known that CVD grown polysilicon recrystallizes in just several minutes upon thermal annealing close to the melting point, their so-called deformation texture could just be the pre-annealed texture.

4.3 Etching versus GND dislocation measurement discrepancy

The possible explanation of the significantly higher GND density recovered by the cross-correlation method is the lower bound GND content noise level, which is estimated to be $\sim 1 \times 10^{12} \text{ m}^{-2}$ with 1×1 binning at $0.5 \mu\text{m}$ step size.^[37] The cross-correlation method has been successfully used to assess the GND density statistically when it is well above this noise floor, however, it may fail to identify the genuine GND density value below this level. When the dislocation density in secondarily recrystallized grains is pronouncedly lower than the detection limit of the cross-correlation method, the value obtained with this characterization method no longer represents the genuine GND content but rather the noise level. The sensitivity of the HR-EBSD method can be increased by average the EBSD patterns over multiple frames^[38] though clearly this would be at the expense of increased data acquisition times. The propagation of error in the lattice rotation measurement into errors in the GND density measurement could be improved by consideration of a larger patch size for the rotation gradient determination as has been utilized by Wallis *et al.*^[39] in studying deformed olivine. However, the increased step size decreases the spatial resolution and may lead to information being lost as a greater fraction of the total dislocation densities contribute to the measured lattice curvatures.^[29]

The lateral width of the etch pits becomes a limitation at higher local dislocation densities as the individual pits eventually merge into a continuous low angle boundary feature. Taking the limiting pit spacing to be $\sim 0.5 \mu\text{m}$ corresponds to misorientation of $\sim 0.4^\circ$, or 8×10^{-3} rads which is readily measured by HR-EBSD, and would lead to a GND density of $\sim 4 \times 10^{12} \text{ m}^{-2}$. Such dislocation arrays are included in the HR-EBSD estimation of GND density, while they tend to be omitted from the etch pitting counting procedures. This factor also contributes to the discrepancies between dislocation densities reported by the two techniques.

4.4 Outlook for photovoltaic applications

The material produced has many regions in which the lowest final dislocation densities (by HR-EBSD) are around 10^{13} m^{-2} or lower (Figure 7), with densities around 10^{11} m^{-2} in localised regions determined by etching. These densities are high in the context of cast multicrystalline silicon, which typically has densities ranging from 10^8 to 10^{10} m^{-2} .^[40] Our densities compare favourably with more novel growth approaches however. For example, thin-film silicon grown on glass by solid-phase crystallisation typically has dislocation densities of order 10^{14} m^{-2} .^[41] Although the dislocation density sometimes correlates inversely with minority carrier lifetime^[42] it has long been known that

the recombination activity of clean dislocations is extremely low.^[43] It is possible that our non-melt based production process will be less susceptible to contamination than other processes, and the next stage of work is to characterise the material in terms of minority carrier lifetime. It is noted that if mechanical deformation were ever to be used to produce silicon wafers then it is vital to minimise contamination occurring via contact points for loading. In our current uniaxial compression set-up loading occurs via high purity alumina rods, with additional small high purity quartz discs placed either side of sample to minimise impurity contamination. A key challenge in developing a future rolling set-up lies in minimising the contamination from the rollers.

5. Summary

The microstructural evolution in Siemens polycrystalline silicon during thermo-mechanical processing has been studied. The starting material was heavily textured with a $\langle 110 \rangle$ fibre structure with grain sizes typically 3 to 30 μm long in growth direction and 1 to 3 μm in diameter. The material contains large twinned grains with $\Sigma 3$ and $\Sigma 9$ grain boundaries and the average GND density is $> 10^{14} \text{ m}^{-2}$, as determined by HR-EBSD. Annealing prior to deformation at 1400 °C leads to an initial 90% recrystallization and a profound reduction in the average GND density to approximately 10^{13} m^{-2} . Deformation at 1150 °C by 10% produces continuous curved high GND content linear structures within grain interiors, presumably in the nature of subgrain boundaries which are essentially dislocation arrays. The GND density stored in these dislocation features is approximately 10^{14} m^{-2} , whereas between them the GND density is lower ($5.0 \times 10^{13} \text{ m}^{-2}$). Annealing at 1400 °C after the deformation facilitates a secondary recrystallization process, resulting in some large grains of 100 μm scale with relatively straight high angle grain boundaries.

HR-EBSD gives the GND density in the final material as $3.2 \times 10^{12} \text{ m}^{-2}$, which is considerably higher than the dislocation density of $5 \times 10^{10} \text{ m}^{-2}$ estimated from etch pit counting. Direct comparison of GND density maps and etched samples showed that when the dislocation density is substantially lower than the detection limit of the cross-correlation method, the value obtained this characterization method no longer represents the genuine GND content but instead reflects the noise level of the HR-EBSD measurement.

Supporting information

Data from this manuscript can be obtained via the authors or can be freely downloaded from <http://wrap.warwick.ac.uk/107829> (URL to be activated when paper accepted).

Acknowledgments

We thank Dr R.J. Falster for provision of the Siemens polycrystalline silicon, L. Walton for assistance with the deformation, and R. Lloyd for assistance with thermal annealing. MW was funded by the China Scholarship Council, JDM by the Royal Academy of Engineering, and JDM and PRW by the EPSRC SuperSilicon PV project (EP/M024911/1).

References

1. H. J. Möller, C. Funke, M. Rinio, S. Scholz, *Thin Solid Films* **2005**, 487, 179.
2. T. Y. Wang, Y. C. Lin, C. Y. Tai, C. C. Fei, M. Y. Tseng, C. W. Lan, *Progress in Photovoltaics: Research and Applications* **2009**, 17, 155.
3. J. M. Serra, J. Maia Alvesa, A. M. Vallera, *Journal of Crystal Growth* **2017**, 468, 590.
4. B. S. Meyerson, *Applied Physics Letters* **1986**, 48, 797.
5. D. M. Powell, J. Hofstetter, D. P. Fenning, R. Hao, T. S. Ravi, T. Buonassisi, *Applied Physics Letters* **2013**, 103, 263902.
6. H. S. Radhakrishnan, R. Martini, V. Depauw, K. Van Nieuwenhuysen, M. Debucquoy, J. Govaerts, I. Gordon, R. Mertens, J. Poortmans, *Physica Status Solidi A* **2014**, 4, 70.
7. H. Lange, I. A. Schwirtlich, *Journal of Crystal Growth* **1990**, 104, 108.
8. J. I. Hanoka, *Solar Energy Materials & Solar Cells* **2001**, 65, 231.
9. P. Bellanger, A. Sow, M. Grau, A. Augusto, J. M. Serra, A. Kaminski, S. Dubois, A. Straboni, *Journal of Crystal Growth* **2012**, 359, 92.
10. B. Pratt, S. Kulkarni, D. P. Pope, C. D. Graham, G. Noel, *Metallurgical Transactions A* **1977**, 8, 1799.
11. S. B. Kulkarni, C. Lall, D. P. Pope, C. D. Graham, *Metallurgical Transactions A* **1980**, 11, 1869.
12. C. Lall, S. B. Kulkarni, C. D. Graham, D. P. Pope, *Materials Science and Engineering* **1981**, 47, 265.
13. N. Mardesich, M. H. Leipold, G. B. Turner, T. G. Digges, *Metallurgical Transactions A* **1979**, 10, 1831.
14. P. Woditsch, W. Koch, *Solar Energy Materials and Solar Cells* **2002**, 72, 11.
15. R. W. Fancher, C. M. Watkins, M. G. Norton, D. F. Bahr, E. W. Osborne, *Journal of Materials Science* **2001**, 36, 5441.
16. M. Seibt, R. Khalil, V. Kveder, W. Schröter, *Applied Physics A* **2009**, 96, 235.
17. J. F. Nye, *Acta Metallurgica* **1953**, 1, 153.
18. M. F. Ashby, *Philosophical Magazine* **1970**, 21, 399.
19. A. Arsenlis, D. M. Parks, *Acta Materialia* **1999**, 47, 1597.
20. A. J. Wilkinson, G. Meaden, D. J. Dingley, *Ultramicroscopy* **2006**, 106, 307.
21. A. J. Wilkinson, G. Meaden, D. J. Dingley, *Materials Science and Technology* **2006**, 22, 1271.
22. P. D. Littlewood, T. B. Britton, A. J. Wilkinson, *Acta Materialia* **2011**, 59, 6489.
23. J. Jiang, T. B. Britton, A. J. Wilkinson, *Philosophical Magazine Letters* **2012**, 92, 580.
24. F. Law, Y. Yi, Hidayat, P. I. Widenborg, J. Luther, B. Hoex, *Journal of Applied Physics* **2013**, 114, 043511.

25. T. Lehmann, C. Reimann, E. Meissner, J. Friedrich, *Acta Materialia* **2016**, 106, 98.
26. M. Wu, DPhil Thesis, University of Oxford, UK **2014**.
27. T. B. Britton, A. J. Wilkinson, *Ultramicroscopy* **2011**, 111, 1395.
28. T. B. Britton, H. Liang, F. P. E. Dunne, A. J. Wilkinson, *Proceedings of the Royal Society A* **2010**, 466, 695.
29. J. Jiang, T. B. Britton, A. J. Wilkinson, *Ultramicroscopy* **2013**, 125, 1.
30. W. J. H. Schins, J. Bezemer, H. Holtrop, S. Radelaar, *Journal of the Electrochemical Society* **1980**, 127, 1193.
31. B. Pratt, S. Kulkarni, D. P. Pope, C. D. Graham, *Journal of the Electrochemical Society* **1976**, 123, 1760.
32. P. Rai - Choudhury, P. L. Hower, *Journal of the Electrochemical Society* **1973**, 120, 1761.
33. W. J. H. Schins, S. Radelaar, *Journal of Materials Science* **1981**, 16, 3153.
34. M. Kinoshita, G. Champier, *Materials Science and Engineering* **1981**, 47, 29.
35. M. Kinoshita, G. Champier, *Scripta Metallurgica* **1979**, 13, 863.
36. C. Schmidt, *Materials Research Bulletin* **1978**, 13, 873.
37. A. J. Wilkinson, D. Randman, *Philosophical Magazine* **2010**, 90, 1159.
38. T. B. Britton, J. Jiang, R. Clough, E. Tarleton, A. Kirkland, A. J. Wilkinson, *Ultramicroscopy* **2013**, 135, 126.
39. D. Wallis, L. N. Hansen, T. B. Britton, A. J. Wilkinson, *Ultramicroscopy* **2016**, 168, 34.
40. M. Al-Amin, J. D. Murphy, *Journal of Applied Physics* **2016**, 119, 235704.
41. J. Huang, S. Varlamov, J. Dore, J. S. Yun, M. A. Green, *Solar Energy Materials & Solar Cells* **2015**, 132, 282.
42. K. Arafune, T. Sasaki, F. Wakabayashi, Y. Terada, Y. Ohshita, M. Yamaguchi, *Physica B* **2006**, 376–377, 236.
43. T. S. Fell, P. R. Wilshaw, M. D. de Coteau, *Physica Status Solidi A* **1993**, 138, 695.

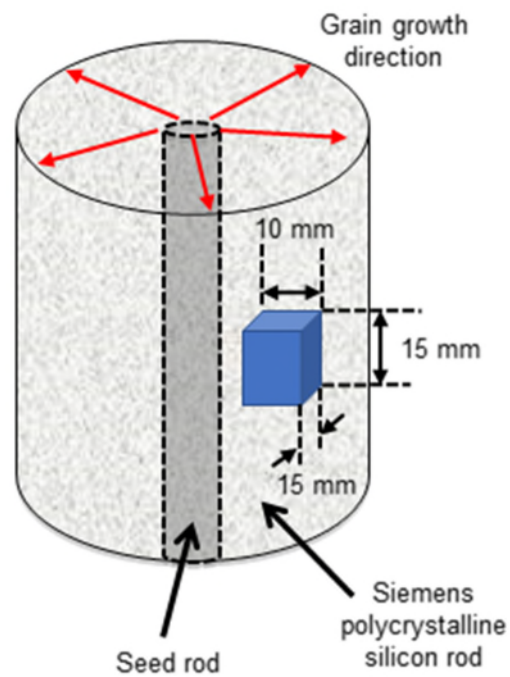


Figure 1. Schematic showing the Siemens rod and the sample orientation. Radial red arrows mark the growth direction. The blue cuboid represents the sample studied, with the 10 mm side coinciding with the growth direction.

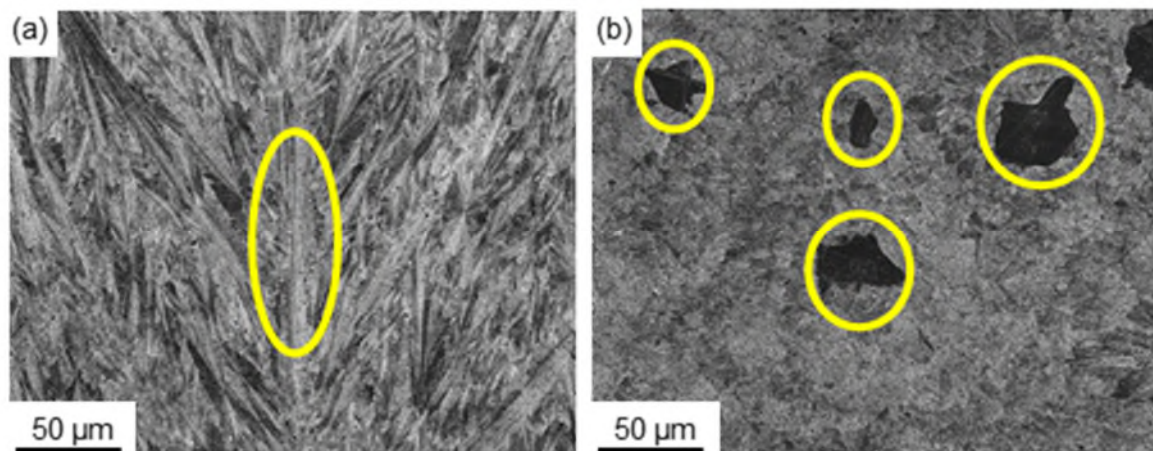


Figure 2. FIB secondary electron micrographs of a preferentially etched surface of as-received Siemens polycrystalline silicon. Image (a) shows a section parallel to the grain growth axis, and image (b) shows a section perpendicular to the grain growth axis. The locations of crystal “tree stems” are indicated.

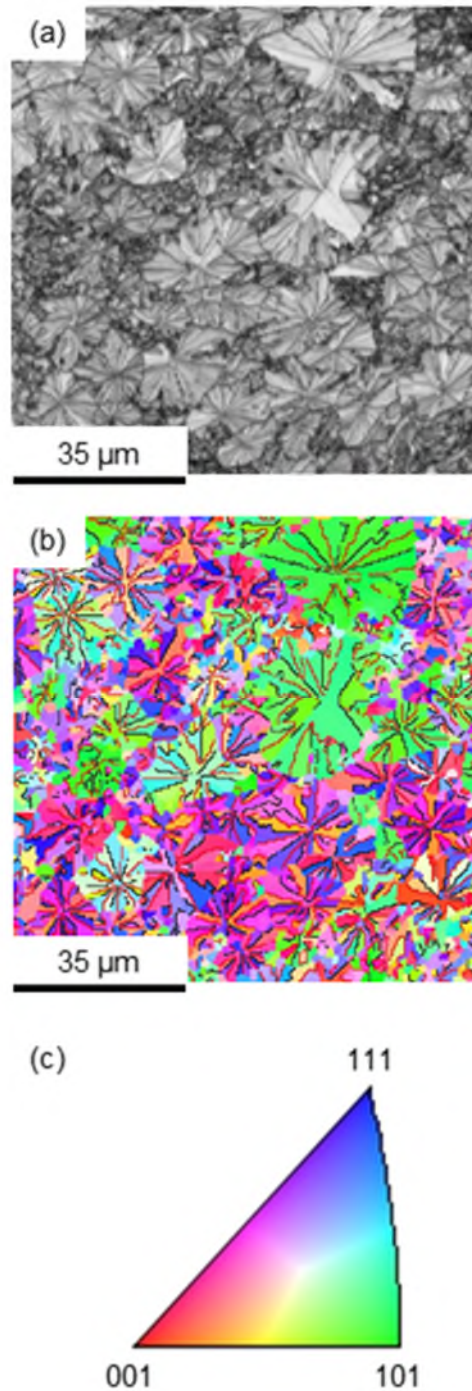


Figure 3. EBSD results for as-received Siemens polycrystalline silicon cut perpendicular to the grain growth axis. Image (a) is an image quality (IQ) map which suggests that grains nucleate at discrete sites and grow outwards radially. Image (b) is an inverse pole figure (IPF) map with $\Sigma 3$ and $\Sigma 9$ twin grain boundaries highlighted in red and black lines, respectively. (c) is the legend for the map in (b).

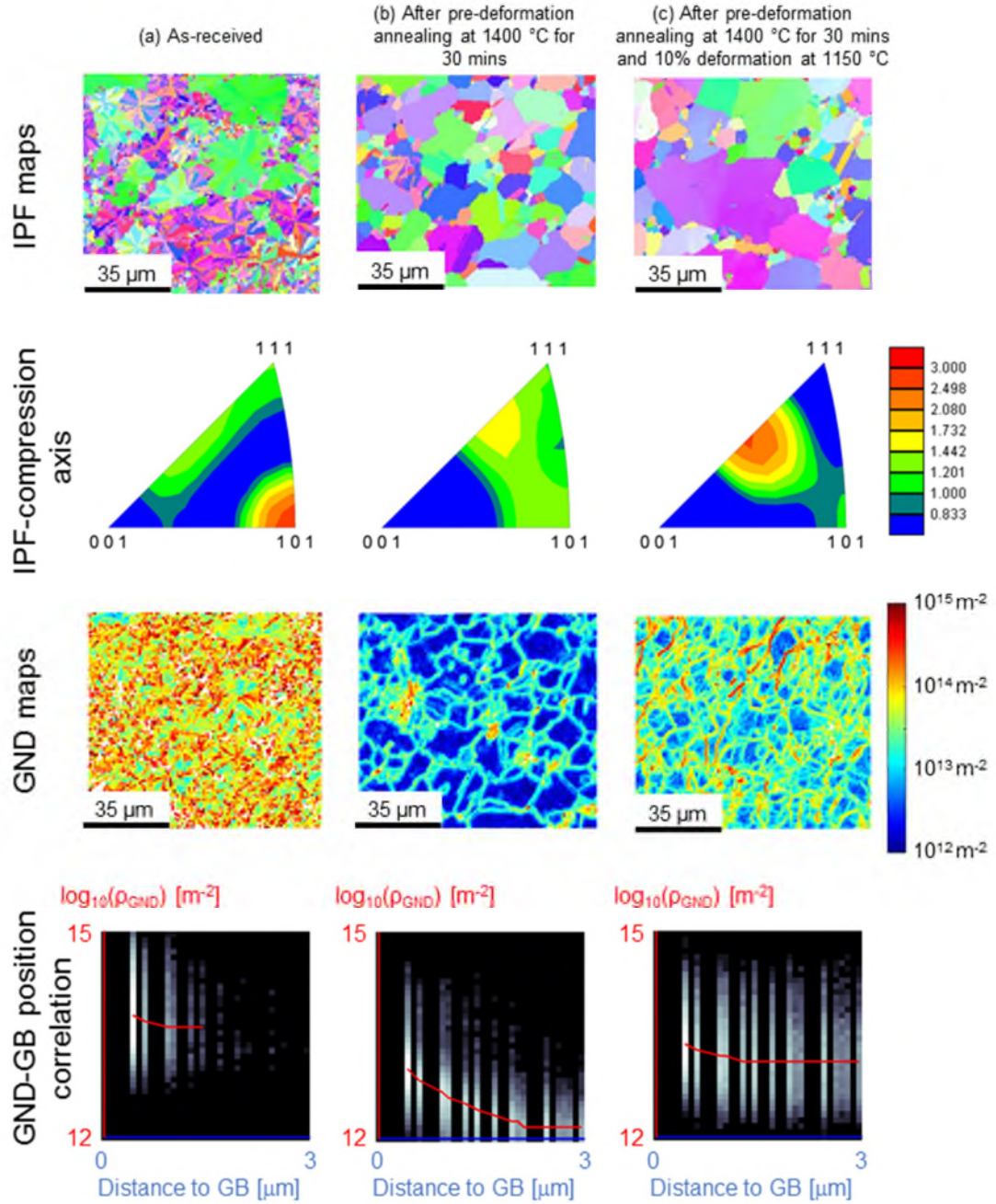


Figure 4. Data from polycrystalline silicon samples from three processing stages. Column (a) is for the as-received state; column (b) is after pre-deformation annealing at 1400 °C for 30 min; and column (c) is after the same pre-deformation annealing followed by compression at 1150 °C by 10 %. First row: IPF maps for the compression axis (coloured according to the IPF in Figure 3 (c)). Second row: IPFs showing crystal direction alignment with the compression axis (a value of 1 corresponds to random orientation, so > 1 or < 1 means more or less likely than randomly expected, respectively). Third row: GND density maps. Fourth row: correlation between GND density and distance to nearest grain boundary (greyscale indicates log of frequency with which combinations of GND density and distance from grain boundary are found, with red line plotting the median GND density as a function of distance from a grain boundary). All map sizes are $100 \mu\text{m} \times 100 \mu\text{m}$ and the scanning step size is $0.5 \mu\text{m}$. White regions in GND density maps correspond to points rejected by cross-correlation quality analysis with $\text{PH} > 0.2$ and mean angular error (MAE) < 0.01 rads.

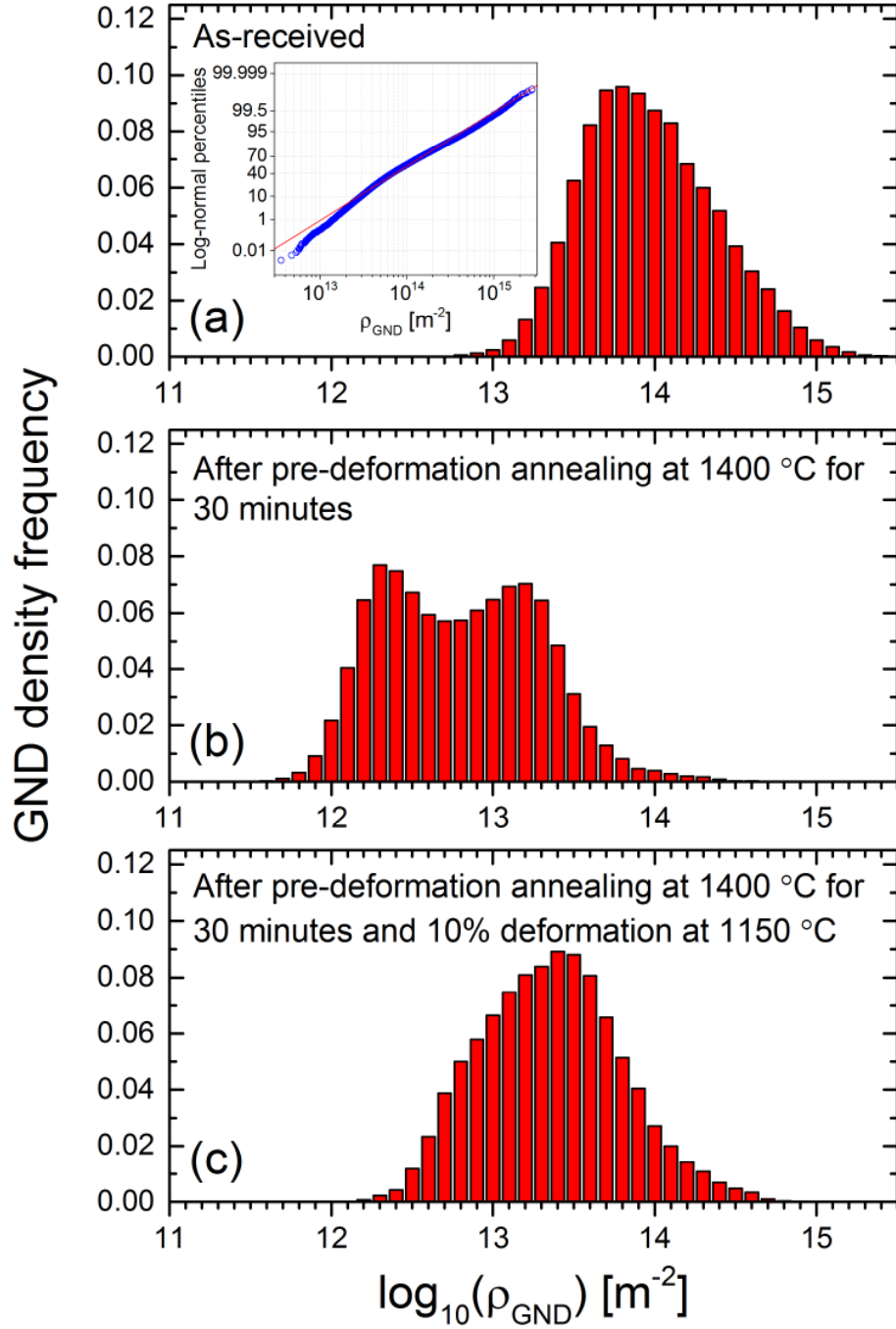


Figure 5. Histograms showing GND density distributions in polycrystalline silicon in: (a) in the as-received state; (b) after pre-deformation annealing at 1400 °C for 30 min; and (c) after the same pre-deformation annealing followed by deformation at 1150 °C by 10 % strain. The inset in (a) demonstrates the distribution in that case is log-normal in nature.

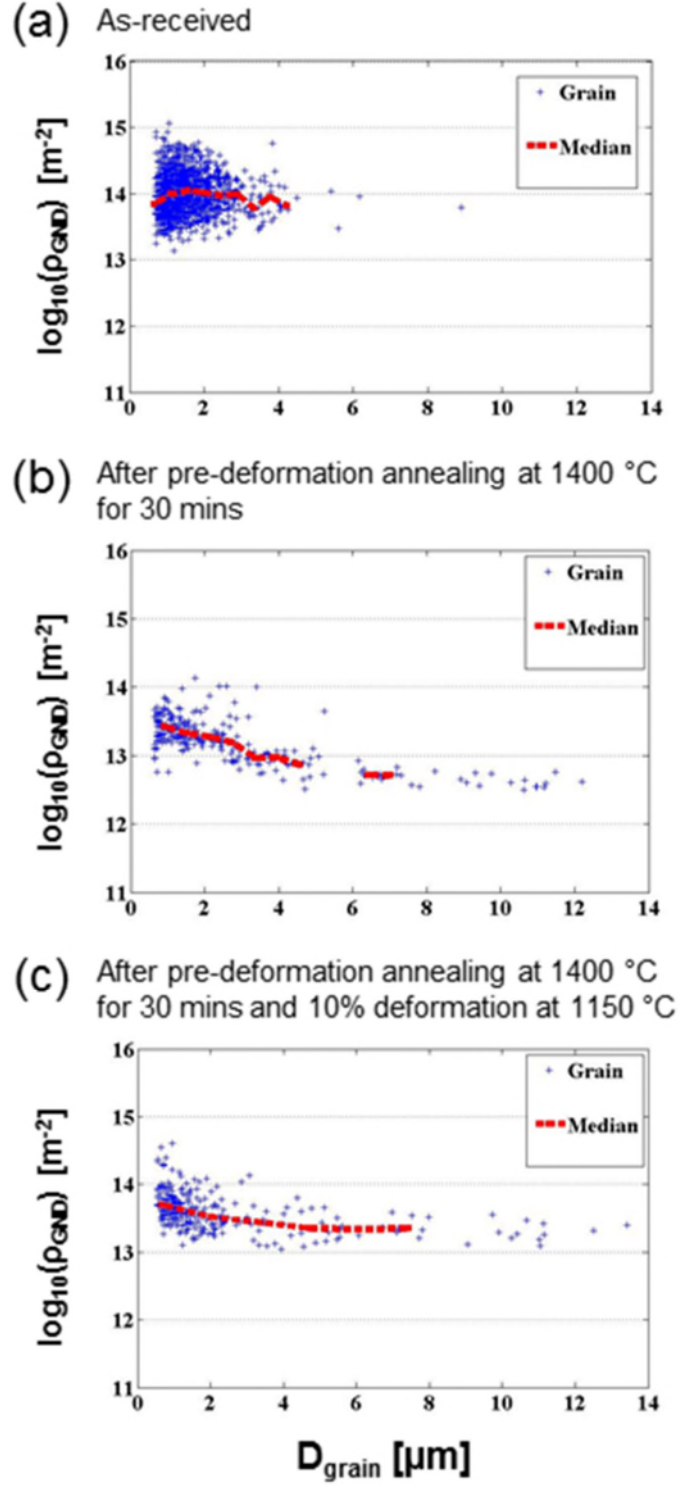


Figure 6. Scatter plot of grain-averaged GND density (in lines per m²) as a function of grain diameter (in μm scale) in polycrystalline silicon in (a) in the as-received state; (b) after pre-deformation annealing at 1400 °C for 30 min; and (c) after the same pre-deformation annealing followed by deformation at 1150 °C by 10 % strain. Marked lines indicate the 10%, 50% and 90% points in the distributions.

Secondary recrystallization:

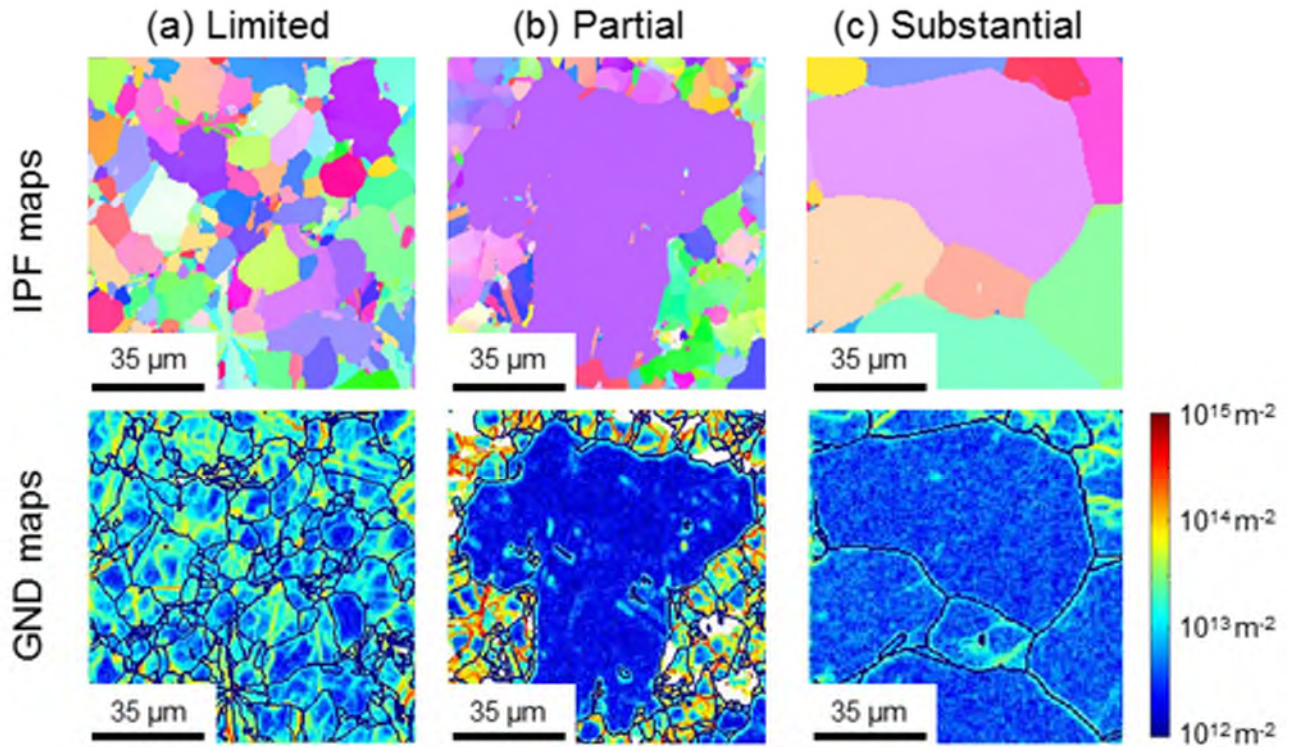


Figure 7. IPF maps and corresponding GND density distribution maps from three different regions of deformed polycrystalline silicon followed by subsequent annealing at 1400 °C for 15 min. Column (a) is from a region in which there is limited secondary recrystallization; column (b) is from a region with partial secondary recrystallization; and column (c) shows a region in which there has been substantial recrystallization. The colouring of the IPF is defined by Figure 3 (c). Dark blue lines on the GND maps represent grain boundaries with minimum misorientation angle of 10° between adjoining pixels. All map sizes are $100 \mu\text{m} \times 100 \mu\text{m}$ and the scanning step size is $0.5 \mu\text{m}$. White regions correspond to the rejected points by cross-correlation quality analysis with $\text{PH} > 0.2$ and $\text{MAE} < 0.01$ rads.

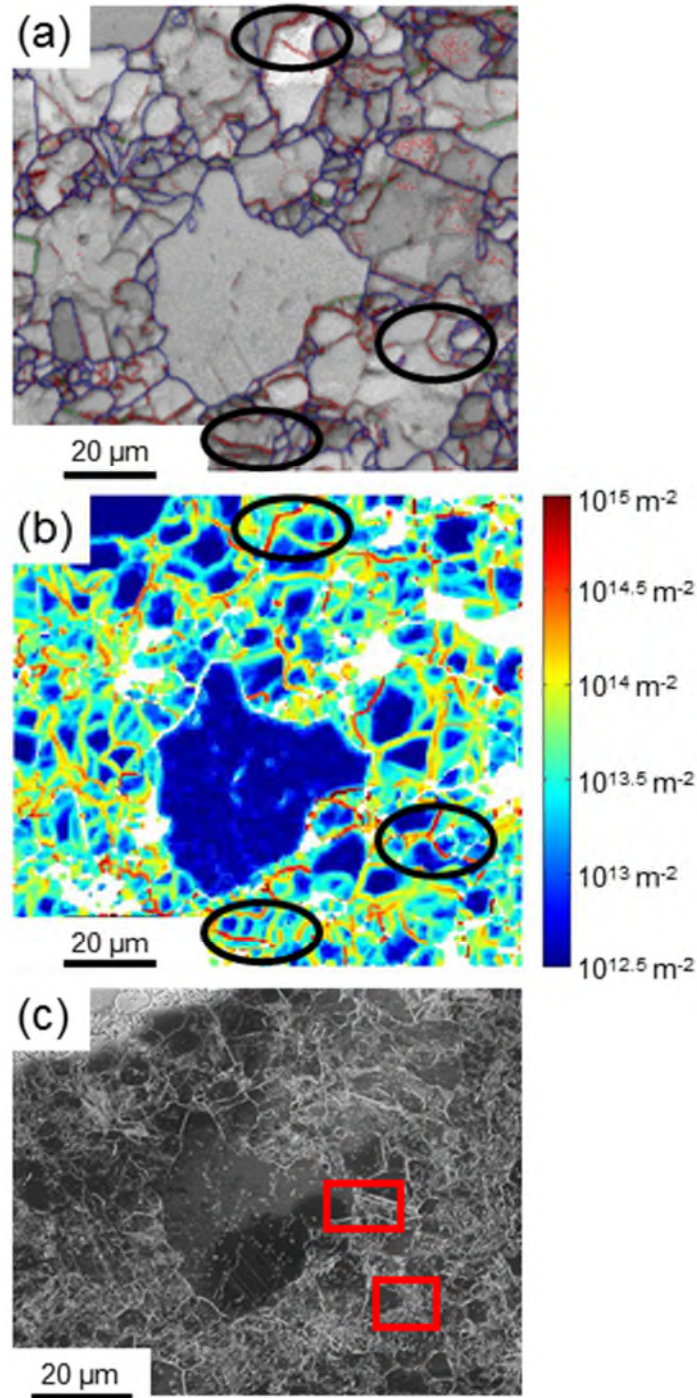


Figure 8. Representative partially recrystallized region with one single individual recrystallized grain from a sample deformed and subsequently annealed at 1400 °C for 15 min: (a) Image quality map with grain boundary type marked using different coloured lines, red lines mark grain boundaries with misorientation between 1° and 5°, green lines mark misorientation between 5° and 15°, and blue lines mark misorientation beyond 15°; (b) Spatial GND density map; (c) FIB secondary electron micrograph post preferential etching by Sirtl etch solution for 30s. Black circles in (a) highlighted the regions containing low angle grain boundaries (misorientations between 1° and 5°) and the corresponding area in spatial GND content map recovered by HR-EBSD cross-correlation method. Red rectangles marked in (c) indicate regions are shown in higher magnification in Figure 9.

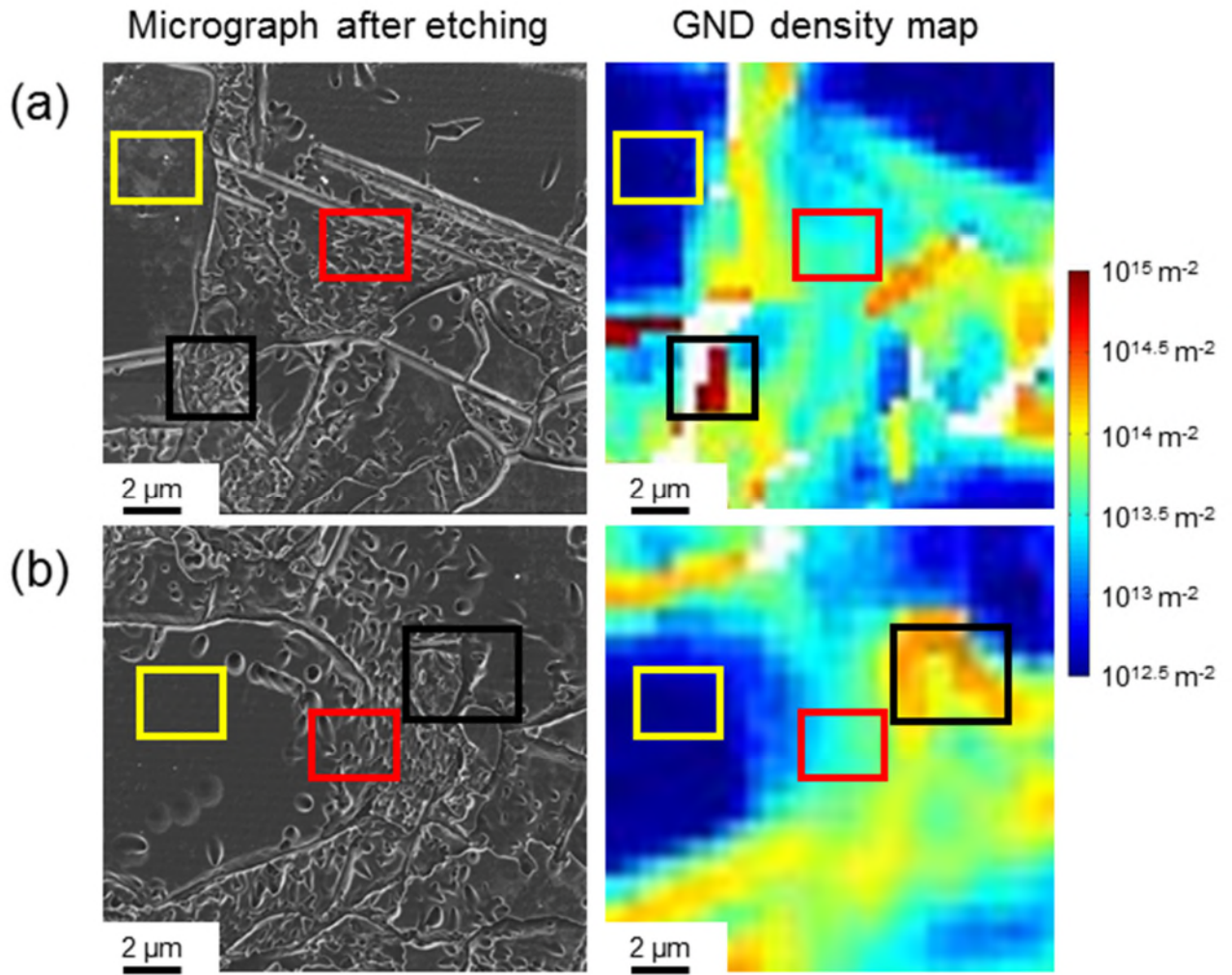


Figure 9. (a) and (c), High magnification FIB secondary electron micrographs; (b) and (d), Corresponding GND density maps of two representative regions in a region which underwent partial secondary recrystallization. Specific low GND density area highlighted by yellow rectangles, medium GND density area marked by red rectangles and high GND density features marked by black rectangles.

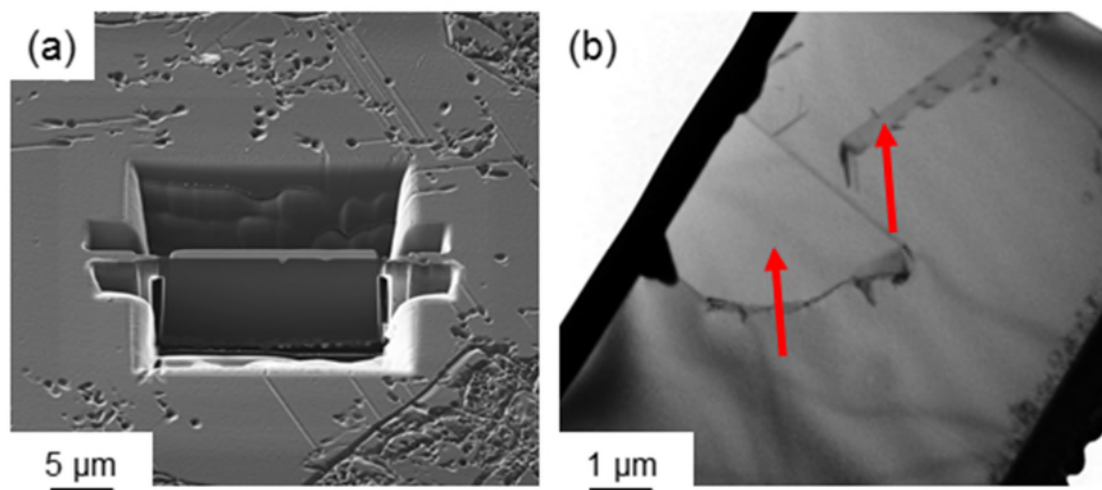


Figure 10. (a) TEM specimen from a region with substantial secondary recrystallization fabricated by a FIB lift-out technique; (b) TEM bright field image taken using (000) spot near [111] zone axis shows that the specimen contains very few crystalline defects. Red arrows mark twin grains.

Table of contents entry

Title: Microstructural evolution of mechanically deformed polycrystalline silicon for kerfless photovoltaics

Keyword: Silicon

Authors: M. Wu, J.D. Murphy, J. Jiang, P.R. Wilshaw, A.J. Wilkinson

Kerfless silicon wafers for photovoltaics could be produced by hot rolling, which motivates this study into the microstructural properties of deformed and annealed polycrystalline silicon. Using high-resolution electron backscatter diffraction deformed polycrystalline silicon feedstock is shown to have 100 μm diameter grains after thermal processing, making it potentially suitable for low-cost photovoltaics provided its electronic properties can be controlled.

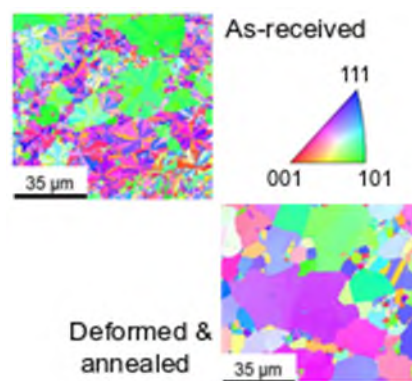


Table of Contents Figure (55 mm \times 50 mm)